





# The effect of surfactants on droplet generation in a plunging breaker

C. Liu<sup>1</sup> , M.A. Erinin<sup>2</sup> , X. Liu<sup>1</sup>  and J.H. Duncan<sup>1</sup> 

<sup>1</sup>Department of Mechanical Engineering, University of Maryland, College Park, MD, USA

<sup>2</sup>Department of Mechanical Engineering, University of Michigan, Ann Arbor, MI, USA

**Corresponding author:** C. Liu, [cliu1213@umd.edu](mailto:cliu1213@umd.edu)

(Received 26 August 2024; revised 27 November 2024; accepted 7 January 2025)

An experimental study is conducted to compare droplet generation in a deep-water plunging breaker in filtered tap water and in the presence of low and high bulk concentrations of the soluble surfactant Triton X-100. The breakers are generated by a programmable wave maker that is set with a single motion profile that produces a highly repeatable dispersively focused two-dimensional (2-D) wave packet with a central wavelength of  $\lambda_0 = 1.18$  m. The droplets are measured with an in-line cinematic holographic system. It is found that the presence of surfactants significantly modifies the overall droplet number and the distributions of droplet diameter and velocity components produced by the four main droplet producing mechanisms of the breaker as identified by Erinin *et al.* (*J. Fluid Mech.*, vol. 967, 2023, p. A36). These modifications are due to both surfactant-induced changes in the flow structures that generate droplets and changes in the details of droplet production mechanisms in each flow structure.

**Key words:** air–sea interactions, wave breaking

## 1. Introduction

Sea spray droplets, which are primarily generated by breaking waves, greatly enhance the rate of transfer of mass, momentum and energy across the air–sea interface (Andreas 1992, 2002; Veron 2015; Deike 2022) and are therefore an important consideration in oceanic and atmospheric physics, and the modelling of weather and climate. Larger sea spray droplets can mediate the heat and momentum fluxes at the ocean–atmosphere interface, and are major players in weather prediction and hurricane intensification (Andreas 1992, 2004; Andreas & Emanuel 2001; Veron 2015). Smaller sea spray droplets can reside in

the marine atmospheric boundary layer for days to weeks, and participate in the global atmospheric aerosol cycle and chemical reactions (Andreae & Rosenfeld 2008).

In small-scale (wavelength  $\lesssim 1$  m) mechanically generated breaking waves, it has been recognised through laboratory and numerical studies that spray droplets are generated via (i) splashing from the impact of the plunging jet and related interface evolution and (ii) the bursting of bubbles that are initially entrained by the breaker, see discussion of these studies below.

Droplet generation by bubble bursting has been explored in both laboratory experiments and numerical simulations for single and collective bubble bursting in cases with otherwise quiescent liquids. These detailed fundamental studies in clean water include Gañán-Calvo (2017, 2018); Gordillo & Rodríguez-Rodríguez (2019); Ghabache & Séon (2016); Blanco-Rodríguez & Gordillo (2020); Lai, Eggers & Deike (2018); Berny *et al.* (2020, 2022); Wang *et al.* (2017); Blanchard & Syzdek (1988); Lhuissier & Villiermaux (2012); Jiang *et al.* (2022), while studies of the effects of surfactants on modifying these processes include Poulain, Villiermaux & Bourouiba (2018); Néel & Deike (2021); Néel *et al.* (2022); Pierre, Poujol & Séon (2022); Constante-Amores *et al.* (2021); Quinn *et al.* (2015); Poulain & Bourouiba (2018); Modini *et al.* (2013); Yang *et al.* (2023). In the above work, Poulain *et al.* (2018); Pierre *et al.* (2022); Constante-Amores *et al.* (2021) further identified the important effect of local surface tension gradients (Marangoni stresses) on droplets production.

There are relatively few numerical or experimental studies of droplet generation in breaking waves. In numerical studies, Wang, Yang & Stern (2016) and Mostert, Popinet & Deike (2022) conducted three-dimensional (3-D) direct numerical simulation (DNS), resolving features ranging in scale from the breaker wavelength ( $\sim 30$  cm) down to the droplet diameters ( $\sim 500$   $\mu\text{m}$ ). In these works, surface tension is commonly modelled by a single parameter that remains constant and uniform on the interface, where Marangoni stress is completely ignored. To the authors' knowledge, no similar calculations in the presence of surfactants have been reported.

In experimental studies, Erinin *et al.* (2019) explored droplet generation in a mechanically generated dispersively focused plunging breaker in filtered tap water and Erinin *et al.* (2023b) further explored the effect of different breaking intensities (wave amplitude) for a single breaker wavelength. They quantified the spatio-temporal distribution of droplet generation in these waves and related the regions of strong generation to local flow structures in the breakers. They also quantified the size and velocity distributions for all the droplets and separately for the droplets produced by each production mechanism. Experiments on droplet generation in shoaling breakers were also reported by Ramirez de la Torre, Petter Vollestad & Jensen (2022), where droplet numbers and diameter distributions were obtained for droplet diameters  $\geq 500$   $\mu\text{m}$  using a cinematic multi-camera visualisation technique.

The current study is an extension of the previous work of Erinin *et al.* (2023c) that used experiments and DNS to explore the effect of surfactants on the profiles of plunging breakers at the moment of jet impact. In this study, it was found that in cases with clean water and water with a very high concentration of the soluble surfactant Triton X-100, the breaker's plunging jet was smooth, two-dimensional (2-D) and extended well forward of the wave's crest, while with lower concentrations of the surfactant, the jet became 3-D and curled inward towards the wave crest. Curves of surface tension versus surface compression (measured with a Wilhelmy plate and a Langmuir trough) and the numerical simulations were used to support the idea that Marangoni stresses found only in the low and intermediate surfactant concentration cases were the cause of the 3-D plunging jet behaviour.

In the present work, we selected two of the most representative surfactant conditions (the lowest and highest concentrations of Triton X-100) from cases presented by Erinin *et al.* (2023c) and conducted detailed cinematic in-line holographic droplet measurements. The droplet production results are presented and compared with those acquired in filtered tap water (no surfactant added) for the same mechanically generated breaker (adapted from Erinin *et al.* 2023b). The surfactant condition with the low concentration of Triton X-100 is a good approximation of biologically active or polluted water commonly found within well-defined, banded sea slicks (Barger, Daniel & Garrett 1974; Modini *et al.* 2013); and the higher concentration is close to the critical micelle concentration (CMC). To the best of the authors' knowledge, measurements of droplet generation in breaking waves in the presence of controlled surfactant conditions have not been previously reported. This study is part of a series of investigations, starting with mechanically generated waves in clean water, and then adding complexity with surfactants (as in the present paper) and wind in future experiments. It is expected that the results of the research programme will be relevant to droplet production in short wavelength ocean waves under conditions with moderate wind forcing.

In the following, the measurement details including the experimental set-up, surfactant solution preparation and maintenance, and holographic measurement details are elaborated in § 2, the droplet spatio-temporal number distributions and droplet size and velocity distributions are presented and discussed in § 3, and the conclusions are given in § 4.

## 2. Experimental details

### 2.1. Wavetank and wave generation

The experimental facilities and droplet measurement techniques used for the present experiments are described in detail by Erinin *et al.* (2023a,b). For completeness, a brief summary of this information is given herein. The experiments were conducted in a wave tank (14.8 m long  $\times$  1.15 m wide  $\times$  2.2 m high) operating with a constant filled water depth of 0.91 m (see figure 1). The deep-water plunging breakers were generated by a programmable wedge-shaped wave maker that produces a highly repeatable dispersively focused 2-D wave packet with an average frequency of  $f_0 = 1.15$  Hz and a corresponding wavelength of  $\lambda_0 = 1.18$  m (by linear theory). A single wave maker motion profile, the one used for the strong breaker case by Erinin *et al.* (2023a,b), was used for all the cases presented in this manuscript. Additional information about this motion profile can be found from Erinin *et al.* (2023a).

### 2.2. Water preparation and surfactant characterisation

In the present study, droplet generation in a breaker generated in filtered tap water (referred to as case Water) and in the presence of two bulk concentrations of the soluble surfactant Triton X-100 (referred to as cases TX1 and TX6a) is compared. The droplet results for the Water case are taken directly from those for the strong breaker of Erinin *et al.* (2023b), while the droplet results for the TX1 and TX6a cases were obtained in the present experiments. Case TX1 corresponds to a Triton X-100 bulk concentration of  $C_{TX} = 2.1 \mu\text{mol L}^{-1}$  (the same as in the TX1 case of Erinin *et al.* 2023c), which creates a contaminated water surface that resembles one sometimes found in the ocean environment. Case TX6a corresponds to  $C_{TX} = 193 \mu\text{mol L}^{-1}$ , which is close to the CMC,  $C_{TX} = 220 \mu\text{mol L}^{-1}$ , as given in the data sheet from the manufacturer, Sigma Aldrich, of the Triton X-100 used in the present study. The value of  $C_{TX}$  in the TX6a case is higher than in the TX6 case of Erinin *et al.* (2023c), where  $C_{TX} = 151 \mu\text{mol L}^{-1}$ . The dynamic

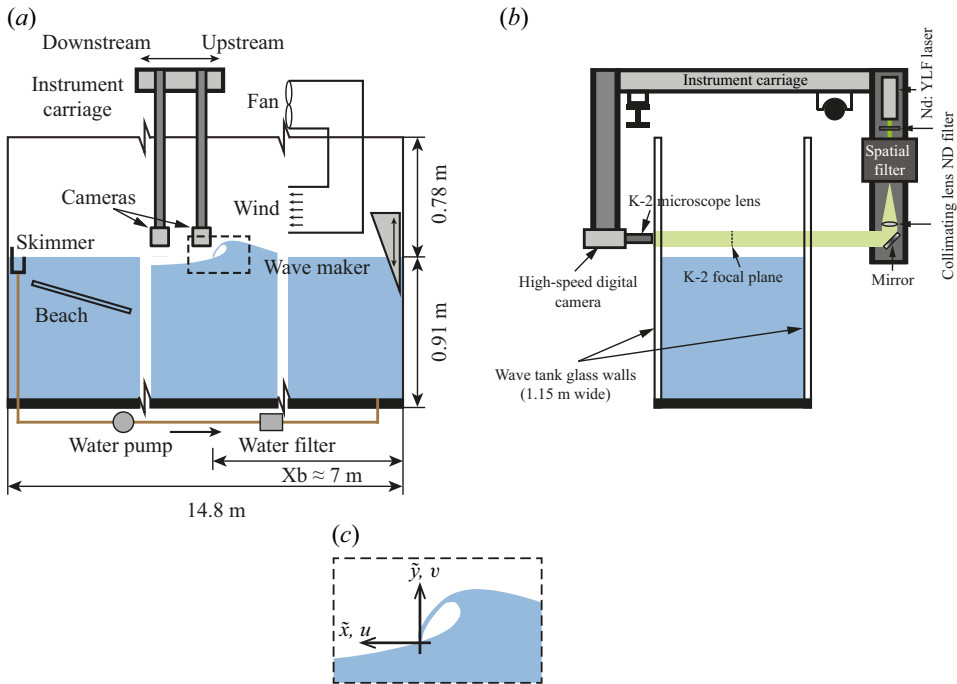


Figure 1. (a) Side-view and (b) end-view schematics of the wave tank and droplet measurement system. The high-speed cameras, lasers and optics are mounted on the instrument carriage, which is translated to various positions along the tank to measure droplets. (c) Coordinate system for the measurements in a schematic drawing of the wave profile at the moment of jet impact. The positive  $\tilde{x}$ -axis is in the downstream direction (in the direction of wave travel) and the positive  $\tilde{y}$ -axis is vertically up. The coordinate origin,  $(\tilde{x}, \tilde{y}) = (0, 0)$ , corresponds to the average jet impact horizontal location and the still water surface height, respectively. The wind system was used during skimming between runs and turned off 15 mins before all measurements.

surface properties of the tank water in each case are characterised by using a Wilhelmy plate and a Teflon Langmuir trough filled with water samples from the wave tank. In this device, the surface tension,  $\sigma$ , is measured by the Wilhelmy plate as Teflon barriers that barely touch the water surface from above compress the water surface area around the plate over a period of 90 s. This compression increases the number of surfactant molecules per unit area between the barriers since the time scale of the surfactant desorption to the bulk is much longer than the compression time, see Chang & Franses (1995); Ferri *et al.* (2008). As the surface concentration increases, the surface tension drops and the resulting curve of  $\sigma(A/A_0)$  is called the surface tension isothermal curve, where  $A$  is the water surface area between the barriers and  $A_0$  is its value before compression, see Erinin *et al.* (2023c) for additional details about the apparatus and measurement techniques.

The surface tension isothermal curves for the three cases studied herein are shown in figure 2. The curves for cases Water and TX1 start ( $A/A_0 = 1.0$ ) from a high ambient surface tension with values of  $\sigma_0 = 72 \text{ mN m}^{-1}$  and  $69 \text{ mN m}^{-1}$ , respectively. As the surface area is compressed, the Water case maintains an almost constant surface tension over 80 % compression (less than  $0.5 \text{ mN m}^{-1}$  reduction in  $\sigma$ ). It is theorised that this behaviour indicates that the surface concentration of surfactant molecules is initially very low, since  $\sigma_0 = 72 \text{ mN m}^{-1}$  is very close to the value for pure water at the tank water temperature, and the concentration is not high enough to change the surface tension until the compression reaches  $A/A_0 = 0.2$ . The surfactant in the Water case is probably produced by bacteria which are known to produce surfactants as byproducts of their

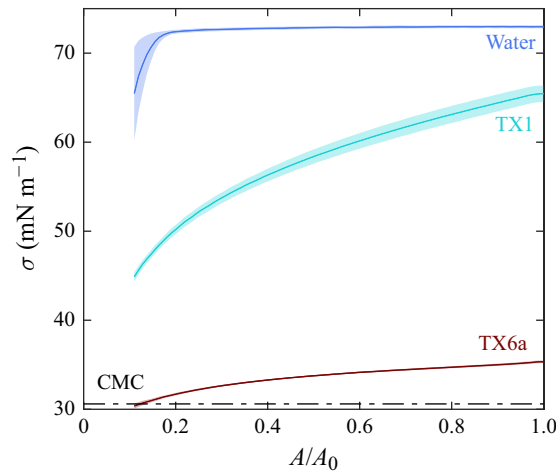


Figure 2. Plot of the measured instantaneous surface tension,  $\sigma$ , versus water surface area ratio ( $A/A_0$ , where  $A_0$  is the initial area) in the Langmuir trough for the Water, TX1 and TX6a cases. The surface area is compressed with a constant speed and the time it takes to decrease  $A/A_0$  from 1 to 0.1 is roughly 90s (barrier velocity  $\approx 100 \text{ mm min}^{-1}$ ). The shaded region in each case encloses all the surface tension curves measured over the entire course of the droplet measurements and the solid lines show the averaged curves. The dash-dotted line indicates the surface tension at the CMC,  $30.6 \text{ mN m}^{-1}$ , see Makievski, Fainerman & Joos (1994).

respiration or is leached from the plastics or sealants used in the wave tank. These unknown surfactants are nearly impossible to remove given the laboratory environment and the large volume of water in the wave tank ( $15.5 \text{ m}^3$ ). The steep slope of the  $\sigma(A/A_0)$  curve for  $A/A_0 < 0.2$  is a property of this unknown surfactant. The TX1 case has a lower ambient surface tension and a much steeper curve than the water case over the range  $1.0 \geq A/A_0 \geq 0.2$ , where  $\sigma$  decreases by  $18 \text{ mN m}^{-1}$ . A small change in  $\sigma$  under surface compression is also found in the TX6a case ( $4 \text{ mN m}^{-1}$  reduction under 80 % compression), although it starts from a significantly lower ambient surface tension ( $\sigma_0 = 35 \text{ mN m}^{-1}$ ) than do the Water and TX1 cases.

Since, as shown by Erinin *et al.* (2023c), the surfactant conditions have a dramatic effect on the breaking behaviour and since the droplet measurements are carried out over a three- to four-week period for each surfactant condition, the following procedures were followed to create and maintain surface conditions as determined by the surface tension isothermal curve during the experiments. At the beginning of the measurements for each TX-100 condition, the tank is first cleaned with highly chlorinated tap water and then filled with tap water via a multi-stage filter system (with pore sizes ranging from 20 microns down to 5 microns). Hypochlorite is then added to bring the chlorine level of the tank water to greater than 10 ppm. The tank water is then skimmed and filtered for a period of approximately 24 h. After the filtration period, the chlorine level is reduced to near zero by adding hydrogen peroxide. This latter step is required to avoid possible chemical reactions between the chlorine and the Triton X-100. The appropriate amount of TX-100 for the TX1 or TX6a case at hand is then mixed with the tank water by turning on the filtration system for a period of approximately three hours. Two protocols have been developed and rigorously followed to maintain a consistent water quality and surface properties during the entire course of the droplet measurements under each surfactant condition. In the first protocol, the following procedures were followed between breaker realisations. Immediately after each breaking event/measurement, the tank water was skimmed and

filtered while the wind tunnel fan was used to blow air towards the skimmer. After 20 mins, the filtration pump and wind tunnel fan were turned off, and then exactly 15 mins was passed to allow water disturbances to decay before making the next wave. The strictly controlled 15-mins calming time also ensured that a consistent amount of surfactant would be adsorbed from the bulk onto the water surface at the moment before running the wave maker. During the skimming period, the Langmuir trough was emptied and rinsed with tap water. At the end of the skimming process, a sample of the tank water was placed in the Langmuir trough. The surface tension isothermal curve was then measured just before the next breaking event. The common wait time for the water in the wave tank and the Langmuir trough allowed for a common adsorption time for surfactants in each facility. The second protocol was implemented when the surface tension isotherm, as measured above, was found to deviate sufficiently from the curve found on the first day of measurements with a given tank of water. In this case, the tank was drained, cleaned and refilled following the above-described procedures. Typically, only one replenishment of the tank water was required for the measurements for each surfactant condition and the shaded region for each curve in [figure 2](#) shows the upper and lower bound for all the measured curves throughout the days of droplets measurements.

### 2.3. Droplet measurements

The droplets are measured with two in-line cinematic holographic systems that are attached to the tank's instrument carriage (see [figure 1](#)). The collimated beam in each system is generated using a high-speed pulsed Nd:YLF laser (CrystalLaser, 527 nm, 500 mW) and associated beam forming optical components. Each system employs a Phantom v641 high-speed camera (resolution  $2560 \times 1600$  pixels<sup>2</sup> and sensor size of) fitted with an Infinity K-2 lens focused on the centreplane of the tank width (image magnification 1 : 1) to record the holograms of the droplets. The laser pulses and image capture times are synchronised to create two sequences of holograms at a rate of 1300 Hz at each measurement location. Additional details about the holographic system can be found from Erinin *et al.* (2023b) and Erinin *et al.* (2023). The hologram measurement volumes span horizontally across the tank width and the bottom surfaces of the two volumes are coplanar and located at a height approximately 1 cm above the highest point reached by the breaking wave crest. The carriage is moved to 20 measurement positions such that the hologram measurement volumes seamlessly cover the streamwise region from the location of plunging jet impact to approximately  $0.89\lambda_0$  downstream. Each recording lasts approximately 2.3 s, corresponding to  $2.645f_0^{-1}$ , after the time of jet impact. The time of jet impact is defined as the time when the tip of the plunging jet (previously in the air) first touches the water surface and the touching point is defined as the jet impact location. The time and location of jet impact is very consistent from run to run and determined by a separate measurement using a laser-induced fluorescence (LIF) imaging technique (see Erinin *et al.* 2023a,c for details). The determination of the time of jet impact normally requires visual inspection of the LIF image sequence and an accuracy of  $\pm 1$  frame ( $\pm 1/650$  s) can be achieved for a single realisation. The variation of time and horizontal location of jet impact over 10 independent runs is found to be within  $\pm 0.01$  s ( $0.9\%$  of  $f_0^{-1}$ ) and  $\pm 2$  cm ( $1.7\%$  of  $\lambda_0$ ), respectively, for each of the three cases presented herein. At each camera location, hologram movies are captured for ten breaking events to provide reasonably well converged statistics for measured quantities, as determined by Erinin *et al.* (2023b) by examining statistics from droplet measurements at two locations for 40 breaking events. In the present experiments, these procedures result in 400 hologram movies captured over a period of approximately three weeks for each wave.



The holograms were reconstructed using a GPU-based Matlab code (Katz & Sheng 2010), which was configured in a parallel computing mode and run on the UMD Zataran High-Performance Computing (HPC) clusters. It has been shown in the work of Erinin (2020) that with the current laser system, camera configuration and in-house code to compute the droplet location and size, droplets with diameters  $d \geq 100 \mu\text{m}$  can be reliably reconstructed with a smaller than 10 % diameter uncertainty for droplets located across the entire width of tank. The droplet trajectories are computed using an in-house droplet tracking code in which the spatial coherence demonstrated by each trajectory is used to reduce the ambiguity confronted when matching the same droplet in subsequent frames (Liu *et al.* 2024). For each of the established trajectories, the associated droplet's diameter ( $d$ ), streamwise location ( $x_d$ ) relative to the horizontal jet impact location, 2-D velocity (streamwise,  $u$  and vertical,  $v$  components) and arrival time ( $t_d$ ) relative to the moment of jet impact is recorded as the droplet travels up across a horizontal plane located 200 pixels from the bottom of each image. The surface created by the corresponding horizontal planes in the holographic space is called the droplet measurement plane and is located approximately 1.2 cm above the highest height reached by the crest of the breaker (12.4 cm above the still water level). The values of  $d$ ,  $x_d$ ,  $t_d$ ,  $u$  and  $v$  form the dataset for these experiments and are used for the analysis and discussion herein. The interested reader is referred to Erinin (2020); Erinin *et al.* (2023) and Liu *et al.* (2024) for additional information about the optical components, holographic reconstruction and droplet tracking.

### 3. Results and discussion

This section is divided into two subsections with § 3.1 describing the three main spatio-temporal regions of droplet production and § 3.2 describing the numbers, diameters and velocities of the droplets generated in each region. The discussion in § 3.2 is organised with a subsection for each droplet producing region where the data for each of the Water, TX1 and TX6a cases are compared, and the effects of surfactants on the associated droplet generation mechanism are discussed. Each data type is presented in a single figure, typically with individual plots for each of the three droplet producing regions. All of the data presented herein for the Water case are from Erinin *et al.* (2023b).

#### 3.1. Droplet producing regions

As the first step in the examination of the droplet dataset, the spatio-temporal distributions of the number of droplets,  $N(\tilde{x}/\lambda_0, \tilde{t}f_0)$ , for the Water, TX1 and TX6a cases are shown in figures 3(a), 3(b) and 3(c), respectively. The coordinates  $\tilde{x}$  and  $\tilde{t}$  are the streamwise horizontal position and time relative to the average position and time, respectively, of jet tip impact  $(\tilde{x}, \tilde{t}) = (0, 0)$  as depicted in the schematic in figure 1(c) and located near the lower right corner in each  $N(\tilde{x}/\lambda_0, \tilde{t}f_0)$  contour plot. See the figure caption for details. Following Erinin *et al.* (2023b), three major droplet producing regions are distinguished as regions I-A, I-B and II, which are shaded by blue, orange and green colour backgrounds, respectively. The locations of the contours of high droplet production in regions I (consisting of region I-A plus region I-B) and II roughly correspond to the locations of the breaking and following wave crests, respectively, as they pass through the measurement region. In region I, the leading edge of the turbulent breaking region roughly corresponds to the lower left edge of the region of high  $N$ . As is discussed in the following subsection, the droplets in regions I-A, I-B and II were found to have been produced by different wave breaking flow structures and droplet generation mechanisms, see Erinin *et al.* (2023b). The breaker in the Water case produces the largest total number

Cases	Water	TX1	TX6a
<b>Region I-A</b> (closure of indent)	241.0(19.8 %) $\pm$ 31	40.8(3.9 %) $\pm$ 13	598.8(52.3 %) $\pm$ 54
<b>Region I-B1</b> (folded indent)	—	118.2(11.3 %) $\pm$ 47	—
<b>Region I-B/I-B2</b> (splashes + large bubbles)	787.4(64.7 %) $\pm$ 53	707.1(67.6 %) $\pm$ 74	542.7(47.4 %) $\pm$ 36
<b>Region II</b> (remaining smaller bubbles)	189.9(15.6 %) $\pm$ 30	179.9(17.2 %) $\pm$ 28	3.4(0.3 %) $\pm$ 4
<b>Total number, <math>N</math></b>	1217 $\pm$ 83	1046 $\pm$ 110	1145 $\pm$ 67

Table 1. Average and standard deviation of the number of droplets generated per breaking event per metre of crest length in regions I-A, I-B and II as well as the total from all regions. Data are given for the filtered tap water case (Water) and the two surfactant cases (TX1 and TX6a). The statistical analysis in the table and subsequent plots is based on 10 times the number of droplets given in any location in the table. In the TX1 case, region I-B is further broken into regions, I-B1 and I-B2. See figure 3 for definitions of these regions. The percent contributions of each region relative to the total number of droplets is given in parentheses.

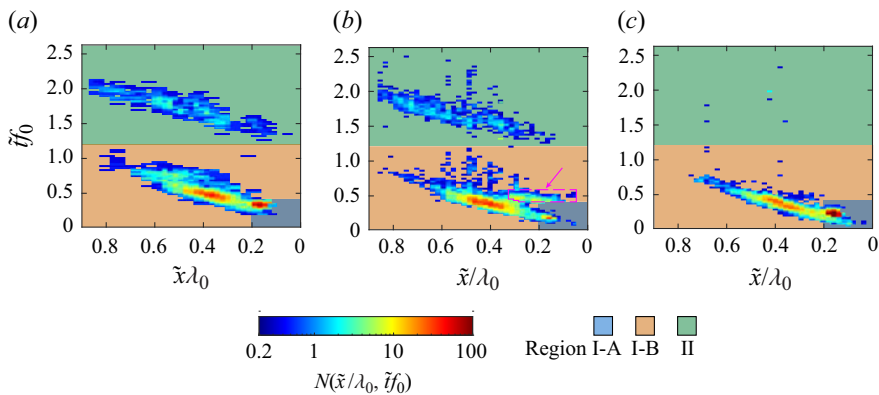
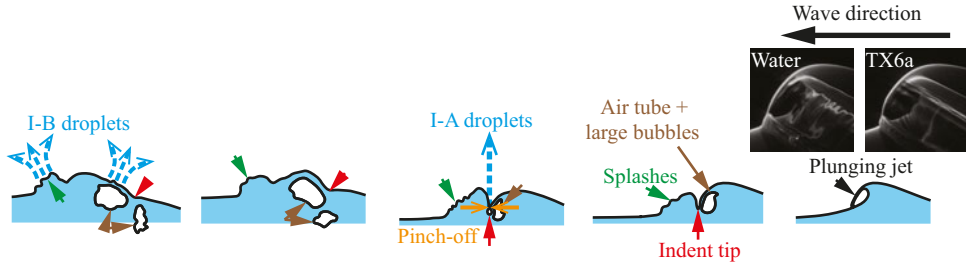


Figure 3. Contour maps of  $N(\tilde{x}/\lambda_0, \tilde{t}/f_0)$ , the number of droplets moving up across the measurement plane per surface area ( $\text{m}^2$ ) per millisecond per breaking event, are shown for the filtered tap water case (Water) and the two surfactant cases (TX1 and TX6a) in panels (a), (b) and (c), respectively. The coordinates  $\tilde{x}$  and  $\tilde{t}$  are the streamwise position and time, respectively, and  $(\tilde{x}, \tilde{t}) = (0, 0)$  is the average position and time of jet impact. The regions identified by the blue, orange and green backgrounds are referred to as I-A, I-B and II, respectively. In panel (b), region I-B is further divided into regions I-B1 (marked by the magenta dashed line) and the remainder of I-B, called I-B2. The data are from at least 10 breaker realisations at each droplet measurement location. The contour maps are shown in the laboratory reference frame and cover the full measurement region ( $\approx 1050$  mm in streamwise distance and  $\approx 2300$  ms in time) with a resolution of  $25.4 \text{ mm} \times 25 \text{ ms}$ . Only droplets with  $d \geq 100 \mu\text{m}$  are counted. The plot in panel (a) is from the strong beaker of Erinin *et al.* (2023b), figure 5(c).

of droplets over the full measurement region (1217), see table 1, and the number reduces to 1046 (14.1 % reduction) and 1145 (5.9 % reduction) in the TX1 and TX6a cases, respectively. Despite these relatively small changes in the total number, the numbers of droplets produced in each region change dramatically with surfactant concentration, see table 1 and the discussion below.



(a)



(b)

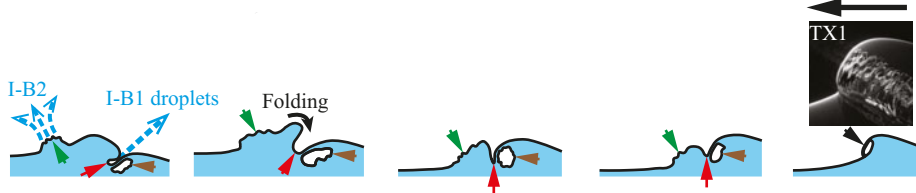


Figure 4. Schematics of the wave profile evolution after the moment of jet impact for the (a) Water/TX6a and (b) TX1 cases. The waves propagate from right to left and the rightmost profile is the moment of jet impact. From right to left, the wave profiles are displayed in a time sequence with a time interval of roughly 0.1 s between schematics in both rows. Region I-A droplets produced in cases Water and TX6a, region I-B1 droplets produced (only) in the TX1 case and region I-B/I-B2 droplets are indicated by the blue dashed arrows in panels (a) and (b). The three LIF images of the wave crests at the jet impact moment are from Erinin *et al.* (2023c).

### 3.2. Droplet characteristics

#### 3.2.1. Region I-A

Region I-A in the  $N(\tilde{x}/\lambda_0, \tilde{t}/f_0)$  contour plots in figure 3 includes the point of jet impact,  $(\tilde{x}, \tilde{t}) = (0, 0)$ , and a short distance downstream and time after. In both the Water and the TX6a cases, a concentrated peak with an extraordinarily large amplitude, which is almost one order of magnitude higher than the next highest peak (found in region I-B in each case), is detected. However, the peak in I-A is much weaker in the TX1 case as seen in figure 3(b). The total numbers of droplets in regions I-A are 241, 41 and 599 in the Water, TX1 and TX6a cases, respectively.

The mechanisms that generate these droplets are visualised in the diffuse-light high-speed videos with above and below surface views of the breakers in supplementary movies 1 and 2, respectively, available at <https://doi.org/10.1017/jfm.2025.65>, and the diagrams in figures 4(a) and 4(b). In each scene of the movies, image sequences for the three cases are shown. In supplementary movie 1, it is clear that the droplets are ejected from the indentation formed between the upper surface of the breaker's plunging jet and the splash that it creates downstream (to the left in the movies). In the Water and TX6a cases, the plunging jets are smooth and nearly 2-D. At impact, smooth nearly 2-D air cavities are formed under the jets, as was also seen in the LIF images labelled as Water and TX6a in figure 4(a). Based on surface tension isotherms under all conditions and numerical calculations of the surface compression distribution along the profile of the plunging jet, Erinin *et al.* (2023c) hypothesised that this similarity in plunging jet characteristics was due to the absence of significant Marangoni stresses in both the Water and TX6a cases. After impact, the tip of the smooth jet in either case penetrates into the water, forming a thin sheet of air in the indentation, see supplementary movie 2. As the jet tip continues to descend into the water, the air sheet becomes thinner due to the differential motion of the adjacent surfaces of the jet and the splash. After a short time, a pinch-off occurs slightly

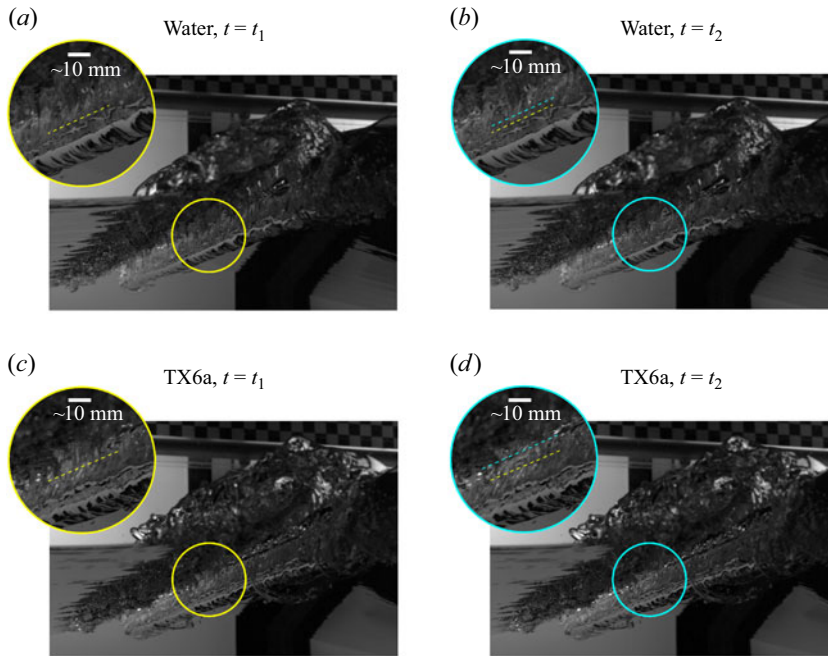


Figure 5. Diffuse light images used for the estimation of the retraction speed of the indentation immediately after pinch-off occurs. Panels (a),(b) and (c),(d) are the two consecutive frames recorded in the Water and TX6a cases, respectively. The time interval between the two frames is  $t_2 - t_1 = 0.769$  ms for both cases. The images were taken with a point of view beneath the water surface with fixed identical camera location and orientation in the two cases, see Movie 2 provided in Supplemental Material for the complete image sequences. Enlarged views in each circled region are provided at the upper left corner in each image. The estimated location of the newly formed indentation tip right after pinch-off occurs is indicated by dashed lines in the enlarged views, with yellow and cyan colour corresponding to the first and subsequent frame, respectively. Toggling between the two frames can aid the determination of the indentation tip location in each one. An estimated length scale representing 10 mm in the enlarged views is denoted in each circle.

above the bottom of the indentation almost simultaneously along a horizontal line in the spanwise direction. After pinch-off, the pinch-off point becomes the tip of the indentation. It then moves rapidly towards the free surface and generates a densely populated sheet of droplets that ejects towards the free surface at the site of the indentation. A small cavity of air is left below the pinch-off point and interacts with the larger cavity that was created under the plunging jet at impact. The entire pinch-off and retraction process is referred to below as the closure of the indentation. This process was first reported for the Water case by Erinin *et al.* (2023b).

Despite the similarities in the plunging jet characteristics, the indentation closure produces 148 % more droplets in the TX6a case than it does in the Water case. It is hypothesised that the large difference is related to differences in the indentation tip retraction speed right after pinch-off,  $V_{rs}$ . Estimates of the speed of retraction of the indentation tip in the Water and TX6a cases are made with the aid of the high-speed diffuse-light image sequences in supplementary movie 2. In each case, two images were used for the estimates and the images for the Water and TX6a cases are given in the first and second rows, respectively, of figure 5. The image pairs show the motion of the pinch-off point between two successive movie frames ( $\Delta t = 0.77$  ms). The estimated spatial resolution in this region of the image is shown in the figure. Using this image resolution

estimate, the accurate time between frames and the indentation tip positions shown in the figure, speeds of  $V_{rs} = 3.9$  and  $8.8 \text{ m s}^{-1}$  were estimated for the Water and TX6a cases, respectively. See figure caption for additional details. The ratio of the indentation tip speeds,  $(V_{rs})_{TX6a}/(V_{rs})_{Water} = 2.26$ , is similar to the ratio of droplet numbers in region I-A,  $N_{TX6a}/N_{Water} = 2.49$ , providing some support for the hypothesis.

In case TX1, as reported by Erinin *et al.* (2023c), the plunging jet is not smooth or 2-D and it curls inward towards the crest as it falls; an irregularly shaped air cavity is formed under the jet at impact. Erinin *et al.* (2023c) hypothesised that these changes occur due to Marangoni stresses that occur because of compression along the jet surface combined with a surface tension that drops continuously and substantially with surface compression. The rough and inward-curling jet is not efficient in penetrating into the water and creating the thin sheet of air in the indentation, as seen in supplementary movie 2 and depicted in figure 4(b). Thus, the entire process of the closure of the indentation found in the Water and TX6a cases is absent, and the total number of droplets generated in region I-A is severely reduced.

The number distribution of the droplet diameter,  $N(d)$ , and the probability density function of the scaled droplet diameter,  $\text{PDF}(d/\ell_c)$ , where  $\ell_c = \sqrt{\sigma_0/(\rho_w g)}$  (with  $\rho_w$  and  $g$  denoting the density of water and the acceleration of gravity, respectively) is the capillary length scale, are shown in figures 6(a) and 6(b), respectively, for all measured droplets and in panels (c) and (d), respectively, for the droplets in region I-A. The values of  $\ell_c$  are 2.7 mm, 2.6 mm and 1.9 mm for the Water, TX1 and TX6a cases, respectively. In figures 6(c) and 6(d), data are given only for the Water and TX6a cases since the number of droplets in the TX1 case was insufficient to produce an accurate distribution. From the plot of  $N(d)$  for region I-A, it can be seen that while the distributions are the same at large diameters, the number of droplets at smaller diameters in the TX6a case is approximately two to five times the number produced in the Water case. However, the PDFs of  $d/\ell_c$  are nearly identical for the Water and TX6a cases, and both have a shape approximated by power laws (straight lines in this log-log plot) in the regions of small ( $d/\ell_c < 0.55$ ) and large ( $d/\ell_c > 0.55$ ) diameters.

PDFs of the velocity components  $u$  and  $v$  for the droplets in region I-A are given in figures 7(a) and 7(b), respectively. As can be seen by comparing the plots, the two components scale quite differently from one another. The PDFs of  $u$  for the two cases, even without any scaling, are almost identical. Both distribution curves for  $u$  are nearly symmetric about  $u = 0$  and are manifested as nearly straight lines on each side of the peak. The PDFs of  $v$  for the Water and TX6a cases, however, are significantly different from one another. The width of the PDF curve for the TX6a case is approximately twice that for the Water case, as is the value of  $v$  at the peak. These data are replotted as the  $\text{PDF}(v/V_{rs})$ , where  $V_{rs}$  is the above-described indentation tip retraction speed, in figure 8(a). As can be seen in the figure, this scaling results in a collapse of the data to nearly the same curve. The success of this scaling lends further support to the above-described estimates of  $V_{rs}$  and, in particular, the ratio  $(V_{rs})_{TX6a}/(V_{rs})_{TX1}$ . In this combined dataset, the average value of  $v/V_{rs}$  is 0.227. The PDFs of  $v$  for the droplets in region I-A for the Water and TX6a cases are further investigated conditioned on droplet diameter with the aid of figure 8(b). In this figure, PDFs of  $v$  for droplets in three diameter ranges ( $100 \leq d \leq 300 \mu\text{m}$ ,  $500 \leq d \leq 700 \mu\text{m}$  and  $900 \leq d \leq 1100 \mu\text{m}$ ) are given, where the PDFs in each size range are computed separately. For the TX6a case, the curves shift to lower ranges of  $v$  as the droplet diameters increase. In contrast, the three velocity distributions in the Water case are all concentrated in lower velocity ranges and form essentially a single curve.

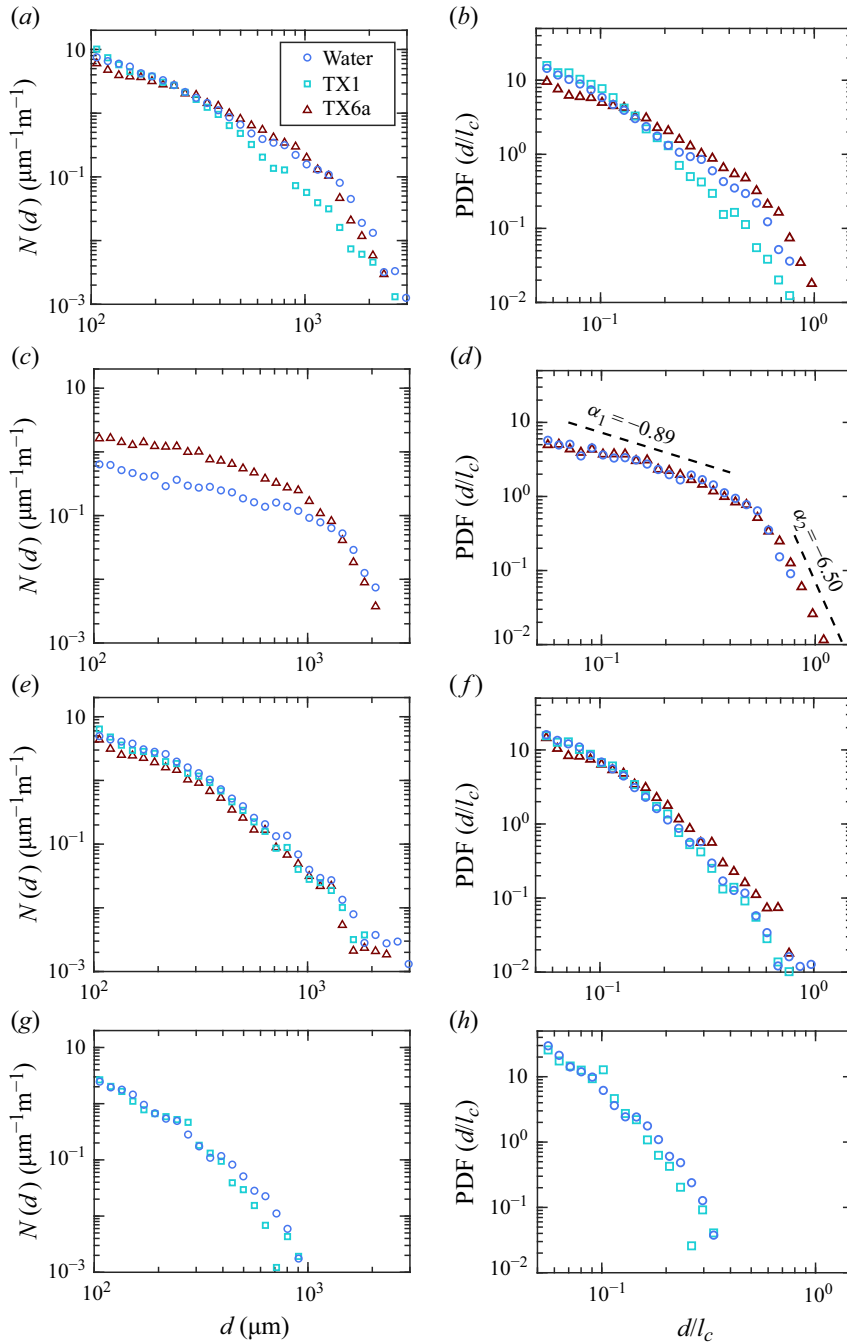


Figure 6. Plots of the number distributions of droplet diameters,  $N(d)$ , are shown in panels (a,c,e,g) and plots of  $\text{PDF}(d/l_c)$  are shown in panels (b,d,f,h), where  $l_c$  is the capillary length scale as defined in the text. The two plots in each row are for droplets in the same region: all regions (a,b); region I-A (c,d); region I-B/I-B2 (e,f); region II (g,h). In the  $N(d)$  subplots, the diameter bins are uniformly spaced on a logarithmic scale, ranging from  $d = 100$  to  $4000 \mu\text{m}$  with a total of 32 bins.  $N(d)$  is computed as the number of droplets counted in each diameter bin normalised by the bin width per meter of crest length and per breaking event. In the PDFs subplots, the normalised diameter bins ( $x$ -axis) are uniformly spaced on a logarithmic scale, ranging from  $d/l_c = 0.05$  to  $1.5$  with a total of 28 bins. The plotting symbol definitions for all subplots are given in the legend in panel (a).

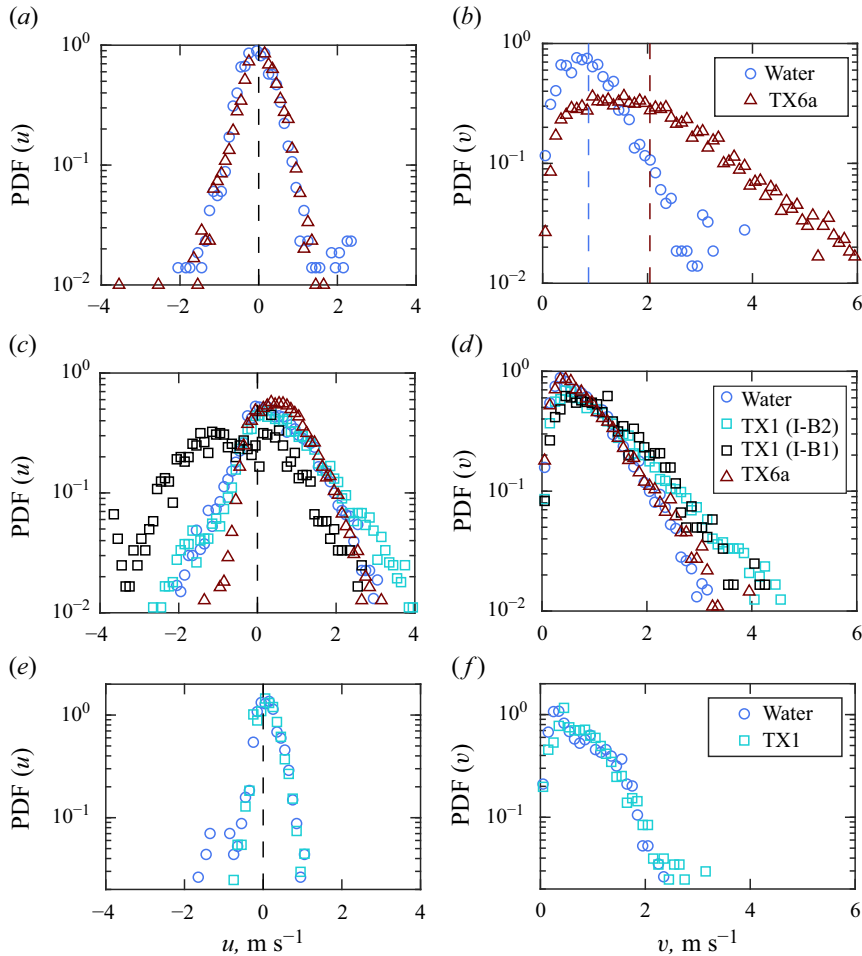


Figure 7. Probability density functions (PDFs) of the horizontal velocity component ( $u$ ; panels *a,c,e*) and vertical velocity component ( $v$ ; panels *b,d,f*) of droplets as they move up through the measurement plane. Positive  $u$  is in the direction of wave propagation. The data covering regions I-A, I-B/I-B2 and II are given in panels (*a,b*), (*c,d*) and (*e,f*), respectively. The width of all bins on the horizontal axis is  $0.1 \text{ m s}^{-1}$  in all panels. The vertical dashed lines in panel (*b*) indicate the averaged vertical velocity in the two cases. In panels (*c*) and (*d*), the PDFs of  $u$  and  $v$  of region I-B1 droplets, which only exist in case TX1, are also presented. In each panel, the plotting symbol definitions are given in the legend in the corresponding row. As in all droplet data presented herein, only the droplets with diameters  $\geq 100 \mu\text{m}$  are sampled in the above plots.

### 3.2.2. Region I-B

Region I-B in the  $N(\tilde{x}/\lambda_0, \tilde{t}f_0)$  contour plots in figure 3 includes the breaking crest from just after the plunging jet impact to the time that the crest leaves the measurement window and excluding region I-A. The contours of  $N$  in region I-B in the Water and TX6a cases are qualitatively similar, both appear as inclined and elongated cigar-shapes that follow the crest of the breaker. In the TX1 case, the main portion of the  $N$  contour is similar to those found in the Water and TX6a cases, but a feature not found in those cases appears as a fork-shaped distribution in the range  $0 < \tilde{x}/\lambda_0 < 0.3$ – $0 < \tilde{t}f_0 < 0.6$ . Within this fork-shaped region, the upper bifurcation, contained in the dashed magenta box, is designated as region I-B1 and the remainder of region I-B is denoted as region I-B2. The notation I-B/I-B2 used

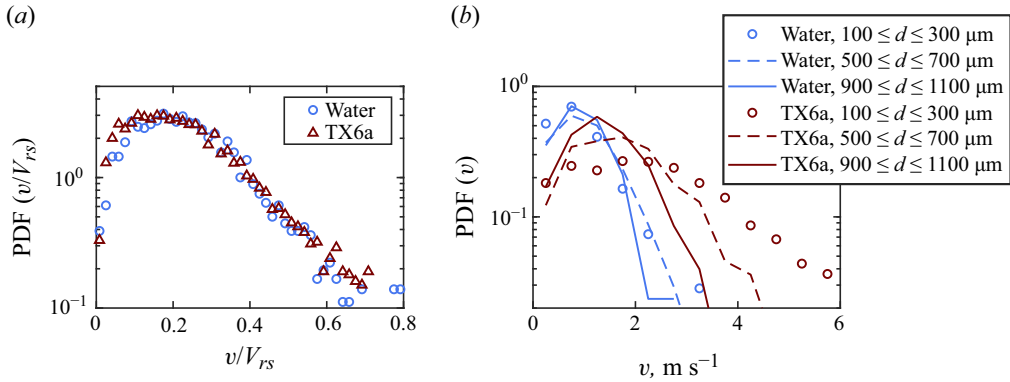


Figure 8. (a) Probability density functions (PDFs) of the scaled vertical velocity component ( $v/V_{rs}$ ) of region I-A droplets, where  $V_{rs}$  is the estimated retraction speed of the indentation tip, which was computed using the method described in the above text with the aid of figure 5. The width of all bins on the horizontal axis is 0.017. (b) The PDFs of  $v$  of region I-A droplets conditioned on three diameter ranges. The width of all bins on the horizontal axis is  $0.5 \text{ m s}^{-1}$ . The plotting symbol definitions are given in the legend in each panel.

below and in some figure captions, refers to region I-B in the Water and TX6a cases and region I-B2 in the TX1 case.

Region I-B/I-B2 droplets are primarily produced by sustained splashing and small bubbles popping near the leading edge of the breaking zone as well as larger bubbles popping on the back face of the breaker crest, see supplementary movie 3. These large bubbles originate from the air cavity entrapped under the plunging jet at impact. Region I-B1 droplets are also produced on the back face of the wave (see supplementary movie 4) and the generation mechanism seems to be a more sudden, energetic and coherent popping of these entrapped large bubbles, which is followed by continued popping of the remaining relatively smaller bubbles. In all three cases, these large bubbles come to the indentation surface created where the upper surface of the plunging jet meets the splash that it generates during the time when the indentation is on the back face of the wave. In the Water and TX6a cases, it appears that the closure of the indentation in some way defocuses the manner in which the large bubbles escape through the surface of indentation.

In region I-B/I-B2, 787 (65 % of the total), 707 (68 %) and 543 (47 %) droplets per breaking event are produced in the Water, TX1 and TX6a cases, respectively, while the number of droplets in region I-B1 in the TX1 case is 118 (11 % of the total). The overall number of droplets in region I-B of the TX1 case (825) is 5 % greater than in the water case.

Plots of  $N(d)$  and  $\text{PDF}(d/\ell_c)$  for region I-B/I-B2 droplets are given in figures 6(e) and 6(f), respectively. The data from the three cases are relatively close to one another in both plots. Also, the curves of  $\text{PDF}(d/\ell_c)$  for the Water and TX1 cases are nearly coincident, perhaps indicating that the associated droplet generation mechanism in this region is only very loosely dependent on the dynamic surface properties.

Figures 7(c) and 7(d) show the PDFs of  $u$  and  $v$ , respectively, for region I-B/I-B2 droplets for the three cases along with region I-B1 droplets in the TX1 case. The averages of the  $u$  velocity components for the Water, TX1 in region I-B1, TX1 in region I-B2 and TX6a cases are  $\bar{u} = 0.44, -0.51, 0.61$  and  $0.63 \text{ m s}^{-1}$ , respectively. The negative value for TX1 region I-B1 droplets is consistent with droplet ejection velocities that are perpendicular to the surface of the back face of the wave, whose unit normal has a horizontal component that is in the direction opposite to the wave propagation. The PDFs of  $v$  for the Water and TX6a cases are similar, with average values of  $0.86$  and  $0.93 \text{ m s}^{-1}$ ,



respectively, as are the PDFs for the TX1 case in regions I-B1 and I-B2, where  $\bar{v} = 1.20$  and  $1.22 \text{ m s}^{-1}$ , respectively. The larger values of  $\bar{v}$  in both sub-regions of I-B in the TX1 case indicate an enhanced energy of splashing and bubble popping, possibly due to the absence of the closure of the indentation process through which a significant amount of energy is probably released.

### 3.2.3. Region II

The contours of  $N$  in region II of the Water and TX1 cases, [figures 3\(a\)](#) and [3\(b\)](#), have inclined and elongated cigar-like shapes that fall on top of the crests of the non-breaking waves that follow the breakers. In both cases, these droplets are generated by the bursting of small entrained bubbles that rise to the surface at the time of passage of the following non-breaking wave, see supplementary movie [5](#). These image sequences indicate that these small bubbles burst all over the surface after the breaker has passed by, but since the droplets have relatively low vertical velocities ([figure 7f](#)), only the bubbles bursting near the crest of the non-breaking wave have a chance of producing droplets that can reach the measurement plane. These processes produce 190 (15.6 % of the total) and 180 (17.2 %) droplets per breaking event in the Water and TX1 cases, respectively. In the TX6a case, many small bubbles come to the water surface during passage of the following wave crest as they do in the Water and TX1 cases; however, in the TX6a case, they remain on the surface without popping in the relatively short time period of measurement ( $\sim 2 \text{ s}$ ). These stable bubbles form patches of foam on the water surface, see supplementary movie [5](#). It is believed that this bubble stability is due to the very high concentration of surfactant molecules in the TX6a case (close to the CMC), as was also reported in studies of collective bubble bursting in surfactant-laden fluids (Modini *et al.* [2013](#); Néel & Deike [2021](#); Néel *et al.* [2022](#)). This lack of bursting bubbles leads to little or no droplet production in region II (comprising only 0.3 % of the total number of droplets per breaking event) and insufficient data for presentation of the droplet diameter and velocity distributions in region II in [figures 6](#) and [7](#), respectively.

From [figures 6\(g\)](#) and [6\(h\)](#) and [7\(e\)](#) and [7\(f\)](#), it can be seen that the droplets in region II for the Water and TX1 cases have similar diameter and velocity ( $u$  and  $v$ ) distributions. The smaller ranges of diameters and velocities found in these distributions indicates that the region II droplets are notably less energetic than those produced in the other two regions. The small bubbles that produce these droplets are carried to the free surface relatively slowly by buoyancy rather than by the more violent flow processes in other parts of the breaking events.

## 4. Conclusions

The results of these experiments indicate that surfactants can dramatically alter the numbers, diameters and ejection velocities of the droplets produced by each of the major droplet generation mechanisms in plunging breakers, which were identified by Erinin *et al.* (2019) and Erinin *et al.* (2023b) as ejection from the thin crater that is formed as a direct result of plunging jet impingement, splashing and small bubbles popping over the turbulent breaking region, the popping of large bubbles on the back face of the breaking crest, and small bubbles popping in the wake of the breaker. In a weak solution of the soluble surfactant Triton X-100 (called herein, TX1), where the surface tension drops rapidly with surface compression, it is found that compared with the case with no added surfactants (called herein, Water), the droplet ejection from the crater is severely diminished, droplet ejection by the large bubbles on the back face of the wave is dramatically enhanced and

droplet generation in the wake is nearly the same. In a concentrated solution of Triton X-100 (called herein, TX6a), the number of droplets from the crater is more than twice that found in the Water case, the number of droplets ejected by large bubble popping on the back face is similar to that in the Water case and the number of droplets ejected over the wake is severely diminished. For the droplets generated from the crater in cases Water and TX6a, the diameter and vertical velocity distribution curves can be collapsed after scaling by the capillary length scale and speed of retraction of the indentation tip, respectively. The current study motivates more sophisticated ocean droplet production models that distinguish and account for the effect of surfactant according to different droplet generation mechanisms. These results pave a way for improved weather and climate models, and advance the studies of aerosol effect on ecosystems in marine and coastal regions.

**Supplementary material and movies.** Supplementary material and movies are available at <https://doi.org/10.1017/jfm.2025.65>.

**Acknowledgements.** The authors thank Professor L. Shen for helpful discussions on droplet generation in breaking waves. The authors thank Professor J. Katz for providing his GPU-based hologram reconstruction algorithm.

**Funding.** The support of the Division of Ocean Sciences of the National Science Foundation under grant OCE1925060 to J.H.D. and X.L. are gratefully acknowledged.

**Declaration of interests.** The authors report no conflict of interest.

**Author contributions.** C.L. and J.H.D. conceptualised and designed the experiments. C.L. collected the data and analysed it with input from J.H.D. and X.L. The paper was written by C.L. with the help of J.H.D. All authors edited the paper.

## REFERENCES

- ANDREAE, M. & ROSENFELD, D. 2008 Aerosol–cloud–precipitation interactions. Part 1. The nature and sources of cloud-active aerosols. *Earth-Sci. Rev.* **89** (1–2), 13–41.
- ANDREAS, E. 2002 A review of the sea spray generation function for the open ocean, *Atmos. Ocean Interactions* **1**, 1–46.
- ANDREAS, E.L. 1992 Sea spray and the turbulent air-sea heat fluxes. *J. Geophys. Res.: Oceans* **97** (C7), 11429–11441.
- ANDREAS, E.L. 2004 Spray stress revisited. *J. Phys. Oceanogr.* **34** (6), 1429–1440.
- ANDREAS, E.L. & EMANUEL, K.A. 2001 Effects of sea spray on tropical cyclone intensity. *J. Atmos. Sci.* **58** (24), 3741–3751.
- BARGER, W.R., DANIEL, W.H. & GARRETT, W.D. 1974 Surface chemical properties of banded sea slicks. In *Deep Sea Research and Oceanographic Abstracts* (ed. M. Sears), vol. **21**, pp. 83–89. Elsevier.
- BERNY, A., DEIKE, L., POPINET, S. & SÉON, T. 2022 Size and speed of jet drops are robust to initial perturbations. *Phys. Rev. Fluids* **7** (1), 013602.
- BERNY, A., DEIKE, L., SÉON, T. & POPINET, S. 2020 Role of all jet drops in mass transfer from bursting bubbles. *Phys. Rev. Fluids* **5** (3), 033605.
- BLANCHARD, D.C. & SYZDEK, L.D. 1988 Film drop production as a function of bubble size. *J. Geophys. Res.: Oceans* **93** (C4), 3649–3654.
- BLANCO-RODRÍGUEZ, F.J. & GORDILLO, J. 2020 On the sea spray aerosol originated from bubble bursting jets. *J. Fluid Mech.* **886**, R2.
- CHANG, C.-H. & FRANCES, E.I. 1995 Adsorption dynamics of surfactants at the air/water interface: a critical review of mathematical models, data, and mechanisms. *Colloids Surf. A: Physico-Chem. Engng Aspects* **100**, 1–45.
- CONSTANTE-AMORES, C.R., KAHOUADJI, L., BATCHVAROV, A., SHIN, S., CHERGUI, J., JURIC, D. & MATAR, O.K. 2021 Dynamics of a surfactant-laden bubble bursting through an interface. *J. Fluid Mech.* **911**, A57.
- DEIKE, L. 2022 Mass transfer at the ocean–atmosphere interface: the role of wave breaking, droplets, and bubbles. *Ann. Rev. Fluid Mech.* **54** (1), 191–224.
- ERININ, M. 2020 The dynamics of plunging breakers and the generation of spray droplets. *PhD thesis*, University of Maryland, USA.

- ERININ, M., LIU, C., LIU, X., MOSTERT, W., DEIKE, L. & DUNCAN, J. 2023c The effects of surfactants on plunging breakers. *J. Fluid Mech.* **972**, R5.
- ERININ, M., LIU, C., WANG, S., LIU, X. & DUNCAN, J. 2023b Plunging breakers. Part 2. Droplet generation. *J. Fluid Mech.* **967**, A36.
- ERININ, M., LIU, X., WANG, S. & DUNCAN, J. 2023a Plunging breakers. Part 1. Analysis of an ensemble of wave profiles. *J. Fluid Mech.* **967**, A35.
- ERININ, M., NÉEL, B., MAZZATENTA, M.T., DUNCAN, J.H. & DEIKE, L. 2023 Comparison between shadow imaging and in-line holography for measuring droplet size distributions. *Exp. Fluids* **64** (5), 96.
- ERININ, M., WANG, S., LIU, R., TOWLE, D., LIU, X. & DUNCAN, J. 2019 Spray generation by a plunging breaker. *Geophys. Res. Lett.* **46** (14), 8244–8251.
- FERRI, J.K., GOREVSKI, N., KOTSMAR, C., LESER, M.E. & MILLER, R. 2008 Desorption kinetics of surfactants at fluid interfaces by novel coaxial capillary pendant drop experiments. *Colloids Surf. A: Physico-Chem. Engng Aspects* **319** (1-3), 13–20.
- GAÑÁN-CALVO, A.M. 2017 Revision of bubble bursting: universal scaling laws of top jet drop size and speed. *Phys. Rev. Lett.* **119** (20), 204502.
- GAÑÁN-CALVO, A.M. 2018 Scaling laws of top jet drop size and speed from bubble bursting including gravity and inviscid limit. *Phys. Rev. Fluids* **3** (9), 091601.
- GHABACHE, E. & SÉON, T. 2016 Size of the top jet drop produced by bubble bursting. *Phys. Rev. Fluids* **1** (5), 051901.
- GORDILLO, J. & RODRÍGUEZ-RODRÍGUEZ, J. 2019 Capillary waves control the ejection of bubble bursting jets. *J. Fluid Mech.* **867**, 556–571.
- JIANG, X., ROTILY, L., VILLERMAUX, E. & WANG, X. 2022 Submicron drops from flapping bursting bubbles. *Proc. Natl Acad. Sci. USA* **119** (1), e2112924119.
- KATZ, J. & SHENG, J. 2010 Applications of holography in fluid mechanics and particle dynamics. *Ann. Rev. Fluid Mech.* **42** (1), 531–555.
- LAI, C.-Y., EGGERS, J. & DEIKE, L. 2018 Bubble bursting: universal cavity and jet profiles. *Phys. Rev. Lett.* **121** (14), 144501.
- LHUISSIER, H. & VILLERMAUX, E. 2012 Bursting bubble aerosols. *J. Fluid Mech.* **696**, 5–44.
- LIU, X., ZHANG, X., ZHENG, Q. & DUNCAN, J.H. 2024 Experimental study on spray in the atmospheric surface layer by raindrops impacting water surface. *J. Fluid Mech.* **988**, R1.
- MAKIEVSKI, A., FAINERMAN, V. & JOOS, P. 1994 Dynamic surface tension of micellar Triton X-100 solutions by the maximum-bubble-pressure method. *J. Colloid Interface Sci.* **166** (1), 6–13.
- MODINI, R., RUSSELL, L., DEANE, G. & STOKES, M. 2013 Effect of soluble surfactant on bubble persistence and bubble-produced aerosol particles. *J. Geophys. Res.: Atmos.* **118** (3), 1388–1400.
- MOSTERT, W., POPINET, S. & DEIKE, L. 2022 High-resolution direct simulation of deep water breaking waves: transition to turbulence, bubbles and droplets production. *J. Fluid Mech.* **942**, A27.
- NÉEL, B. & DEIKE, L. 2021 Collective bursting of free-surface bubbles, and the role of surface contamination. *J. Fluid Mech.* **917**, A46.
- NÉEL, B., ERININ, M. & DEIKE, L. 2022 Role of contamination in optimal droplet production by collective bubble bursting. *Geophys. Res. Lett.* **49** (1), e2021GL096740.
- PIERRE, J., POIJOL, M. & SÉON, T. 2022 Influence of surfactant concentration on drop production by bubble bursting. *Phys. Rev. Fluids* **7** (7), 073602.
- POULAIN, S. & BOUROUIBA, L. 2018 Biosurfactants change the thinning of contaminated bubbles at bacteria-laden water interfaces. *Phys. Rev. Lett.* **121** (20), 204502.
- POULAIN, S., VILLERMAUX, E. & BOUROUIBA, L. 2018 Ageing and burst of surface bubbles. *J. Fluid Mech.* **851**, 636–671.
- QUINN, P.K., COLLINS, D.B., GRASSIAN, V.H., PRATHER, K.A. & BATES, T.S. 2015 Chemistry and related properties of freshly emitted sea spray aerosol. *Chem. Rev.* **115** (10), 4383–4399.
- RAMIREZ DE LA TORRE, R., PETTER VOLLESTAD, P. & JENSEN, A. 2022 Experimental investigation of droplet generation by post-breaking plunger waves. *Water Waves* **4** (1), 1–21.
- VERON, F. 2015 Ocean spray. *Ann. Rev. Fluid Mech.* **47** (1), 507–538.
- WANG, X. et al. 2017 The role of jet and film drops in controlling the mixing state of submicron sea spray aerosol particles. *Proc. Natl Acad. Sci. USA* **114** (27), 6978–6983.
- WANG, Z., YANG, J. & STERN, F. 2016 High-fidelity simulations of bubble, droplet and spray formation in breaking waves. *J. Fluid Mech.* **792**, 307–327.
- YANG, Z., JI, B., AULT, J.T. & FENG, J. 2023 Enhanced singular jet formation in oil-coated bubble bursting. *Nat. Phys.* **19** (6), 1–7.